LETTERS
PUBLISHED ONLINE: 20 NOVEMBER 2011 | DOI: 10.1038/NMAT3170
nature materials

Atomic-scale transport in epitaxial graphene

Shuai-Hua Ji*, J. B. Hannon, R. M. Tromp, V. Perebeinos, J. Tersoff and F. M. Ross*

The high carrier mobility of graphene[1–4] is key to its applications, and understanding the factors that limit mobility is essential for future devices. Yet, despite significant progress, mobilities in excess of the 2×10^5 cm^2 V^{-1} s^{-1} demonstrated in free-standing graphene films[5,6] have not been duplicated in conventional graphene devices fabricated on substrates. Understanding the origins of this degradation is perhaps the main challenge facing graphene device research. Experiments that probe carrier scattering in devices are often indirect[7], relying on the predictions of a specific model for scattering, such as random charged impurities in the substrate[8–10]. Here, we describe model-independent, atomic-scale transport measurements that show that scattering at two key defects—surface steps and changes in layer thickness—seriously degrades transport in epitaxial graphene films on SiC. These measurements demonstrate the strong impact of atomic-scale substrate features on graphene performance.

Our results are based on scanning tunnelling potentiometry to measure local electric potential as current flows through a graphene film. By measuring local perturbations caused by substrate steps and changes in graphene thickness, we demonstrate that such heterogeneity is critical to transport in graphene. Substrate steps alone can increase the resistivity several-fold relative to a perfect terrace, and direct calculation shows that resistance arising from the intrinsic wavefunction mismatch will always exist at junctions between monolayer and bilayer graphene. The performance of graphene devices on SiC surfaces is thus fundamentally limited by the ability to control both the layer thickness and substrate perfection.

Figure 1a and b show low-energy electron microscopy (LEEM) images obtained immediately after graphene growth on two SiC(0001) substrates with different step densities (see Methods). The graphene thickness can be determined straightforwardly with LEEM from the reflectivity of the low-energy electrons, which depends on thickness through quantum confinement effects[11]. In Fig. 1a the sample consists of ~80% monolayer graphene (grey regions labelled 1), ~10% 'buffer' layer that has a C-rich $6\sqrt{3} \times 6\sqrt{3}$ structure (white regions) and ~10% bilayer graphene (dark regions). In Fig. 1b the fractions of monolayer and bilayer graphene (labelled 1 and 2 respectively) are almost equal. Identifying by atomic-resolution scanning tunnelling microscopy (STM) the same areas that were imaged by LEEM enables us to characterize monolayer, bilayer and buffer-layer graphene. Consistent with other work[12–14], each has a distinctive appearance (Fig. 1c,d). Because substrate and graphene step configurations can be determined through STM height measurements, we can obtain a comprehensive picture of nanoscale topography.

In Fig. 1e, we show the experimental approach used to obtain maps of the electrical potential through scanning tunnelling potentiometry[15,16]. Two static probes (1 and 3) contact the surface at a separation of ~500 μm. A voltage applied between these probes induces current flow through the graphene sheet, while a third, scanning probe (2) measures the local potential.

The potential can be measured on the macroscale, by stepping probe 2 across the surface, or on the microscale, by scanning probe 2 over a smaller area, in which case the topography of the sample can be acquired simultaneously. (Note that traditional four-probe measurements require all probes to contact the surface.) Figure 1f shows the macroscale potential. The total resistance (including the contact resistance and the resistance of the graphene sheet) and total current passing through the graphene are also measured. The potential distribution in this two-dimensional system is then modelled[16] as a Laplace problem with fixed boundary conditions at the tips (see Methods). By fitting the potential acquired along the line between probes 1 and 3, macroscopic conductivities σ_{avg} can be determined for the two samples (Table 1).

In Fig. 2, we show microscale potential measurements over regions measuring hundreds of nanometres. The topography and graphene thicknesses are shown in Fig. 2a. Without applying a voltage between probes 1 and 3, the potential map (Fig. 2d) is almost featureless, as expected. But when a voltage is applied (Fig. 2b,e), the maps show two distinct features: dramatic potential jumps at the step edges, and a potential gradient on the terraces. These effects change sign when the applied voltage is reversed (Fig. 2c,f), showing that the measurement is directly related to transport.

The terrace gradient demonstrates that graphene terraces have a finite conductivity, presumably due to random scattering sources at the terraces (such as defects[13], long-range scattering[7–10] or phonons[6]) and at the interface[17], but the potential discontinuity at the step edges indicates additional scattering at these locations. Carrier scattering seems to be particularly strong at the heterogeneous junctions between monolayer and bilayer graphene, and weaker but still visible at locations where a uniform graphene bilayer crosses a substrate step (top right corner of each map). Potential profiles across two terraces and a monolayer–bilayer junction are shown for a series of applied voltages in Fig. 2i,j. The linear relationships between the terrace gradient and monolayer–bilayer jump and the applied voltage are demonstrated in Fig. 2k.

On the terraces, the linear dependence of slope on applied voltage suggests that the terraces are behaving Ohmically: the local electric field $\underline{E}$ (the potential change per unit length) is related to the local current density j by $j = \sigma_t \underline{E}$, where σ_t is a constant (but local) terrace conductivity. We cannot measure the current density locally. However, we can estimate it by noting that all measurements were made approximately half way between the fixed probes, where the average current density can be calculated from the measured total current using the Laplace equation above. The local current density may differ somewhat from the average current density, but this approach enables us to estimate local terrace conductivities for monolayer graphene (Table 1). (Bilayer graphene shows similar resistivity to monolayer graphene, as can be inferred for example from Fig. 2i,j.) On the basis of

IBM T. J. Watson Research Center, Yorktown Heights, New York 10598, United States. *e-mail: jishuaihua1980@gmail.com; fmross@us.ibm.com.

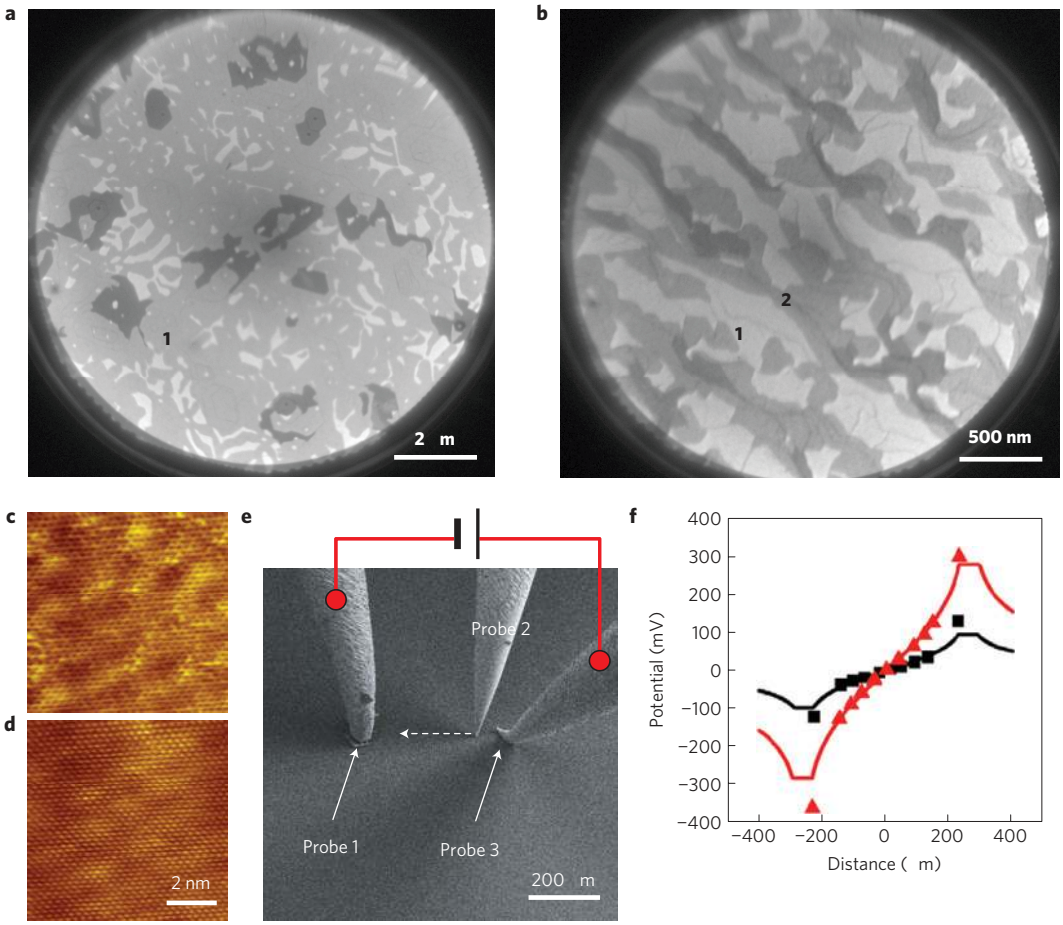

Figure 1 | LEEM, STM and macroscale potential measurement of graphene on SiC. a, Bright-field LEEM image of graphene on 0.06°-miscut 4H SiC(0001), field of view 10 μm. **b**, Bright-field LEEM image of graphene on 0.5°-miscut 6H SiC(0001), field of view 3 μm. **c**, STM of monolayer graphene (STM bias voltage $V = -0.05$ V, tunnelling current $I = 0.1$ nA) showing a honeycomb structure with a moiré pattern; roughness induced by the interface also evident. **d**, STM of bilayer graphene ($V = -0.05$ V, $I = 0.1$ nA) showing a hexagonal structure and smoother surface. **e**, Scanning electron microscopy image of the scanning tunnelling potentiometry experiment. An a.c. voltage V_{13} ($V_{r.m.s.} = 2$ mV, frequency $f = 2$ kHz) is applied between fixed probes 1 and 3 to maintain scanning probe 2 in the tunnelling range, measuring through a feedback loop the potential when no net current flows at probe 2. **f**, Potential measured (at ~72 K) by stepping probe 2 across the surface to points along the dashed line in **e** with positions determined with scanning electron microscopy. Black square data points were measured on the low-miscut sample at $V_{13} = 252$ mV; the total current is 0.906 mA and hence resistance is 276 Ω. Red triangular data points are for the high-miscut sample, where the measured resistance is larger (722 Ω) at the same probe spacing; $V_{13} = 659$ mV was used to achieve the same total current. Solid lines are the results of fitting a two-dimensional calculation of current flow using probe contact areas of 60 μm.

scanning tunnelling spectroscopy results also obtained on these samples (Supplementary Fig. S1) and angle-resolved photoemission spectroscopy measurements from the literature[18,19], we estimate the electron density in the monolayer graphene to be $\sim 10^{13}$ cm^{-2} and the local mobility for monolayer graphene on terraces at 72 K to be $\sim$3,000 cm^2 V^{-1} s^{-1} in both samples.

The monolayer–bilayer graphene junction also obeys Ohm's law (Fig. 2k): the linear dependence of voltage jump ΔV on applied voltage and hence local electric field indicates that ΔV is also proportional to the local current density, that is, $\Delta V \propto j$. With the local current density j estimated as above, the monolayer–bilayer junction resistance ρ_{step} can be extracted (Fig. 3d) using $V = j\rho_{step}$.

Where a single, continuous layer of graphene crosses a substrate step, the effect is weaker but still quantifiable. In Fig. 3a,b, single-layer graphene crosses 0.5-nm-high substrate steps. Although the potential discontinuity at the steps is hard to discern in individual scan lines (Fig. 3b), averaging shows the magnitude of the effect (Fig. 3c). It is also clear from Fig. 3c that higher steps show a greater potential jump (for similar terrace gradient and hence local current density). Ohm's law is followed (Supplementary Fig. S2), so values for the step resistance ρ_{step} can be calculated. Although changes in graphene conductance near steps have been described[20], this technique provides a quantitative measure of the extra resistance.

Table 1 | Conductivity of graphene on SiC substrates with different miscut angles.

	Low miscut (~0.06°)	High miscut (0.5°)
Average conductivity σ_{avg} from macroscale measurement (mS)	4.32 ± 0.09	1.46 ± 0.03
Conductivity of monolayer graphene σ_t from microscale measurement (mS)	5.0 ± 0.7	4.4 ± 0.7

Figure 3d summarizes the results for monolayer graphene crossing substrate steps, and for monolayer–bilayer junctions of different configurations. Monolayer graphene crossing single (0.5 nm) substrate steps shows a resistance of 6.9 ± 2.9 Ω μm. The resistance seems to increase linearly with step height, 14.9 ± 3.6 Ω μm for

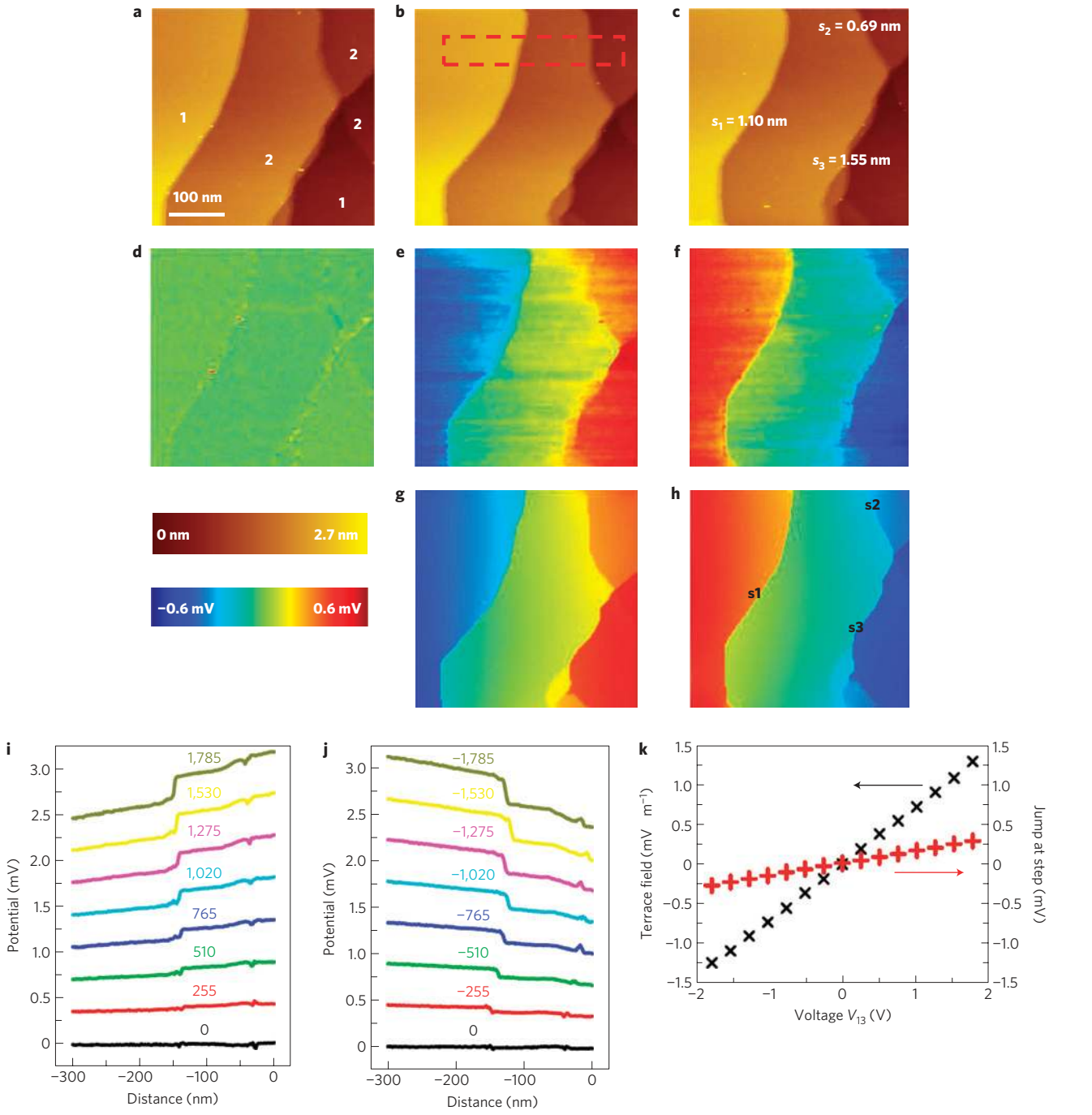

Figure 2 | Scanning tunnelling potentiometry of terraces and monolayer–bilayer junctions. a–f, Topography (**a–c**) and potential maps (**d–f**) recorded simultaneously (a.c. voltage $V_{a.c.} = 2$ mV, $I = 50$ pA; room temperature) with $V_{13} = 0$ (**a**,**d**), $V_{13} = 1.53$ V and total current 5.73 mA (**b**,**e**) and $V_{13} = -1.53$ V (**c**,**f**). The voltage range is shown on the colour scale; zero is arbitrary. The step heights and graphene thickness (labels in **a** and **c**) are identified from STM. The local current density midway between the fixed probes is 4×10^{-6} A μm^{-1}. **g**,**h**, Simulated potential maps calculated using the experimental boundary potential conditions. Step edges s_1, s_2 and s_3 have resistances of 41, 13 and 69 Ω μm respectively. **i**,**j**, Line profiles of the potential averaged from the rectangle in **b**, shown for the V_{13} values indicated (mV). Data are offset vertically for clarity. The terrace slopes on the monolayer and bilayer sides are similar for each voltage, suggesting that the resistivity of the bilayer graphene is similar to that of the monolayer graphene in this region. **k**, The electric field on the terraces (slopes in **i** and **j**; monolayer and bilayer terraces being similar) and the potential jump at the monolayer–bilayer junction (jump heights in **i** and **j**) as a function of V_{13}.

1.0 nm steps and 24.7 ± 4.3 Ω μm for 1.5 nm steps. One example of bilayer graphene crossing a step is also included, and it follows the same trend. Monolayer–bilayer junctions have a higher resistance, 20.9 ± 5.7 Ω μm and 28.4 ± 7.0 Ω μm for planar and stepped junctions respectively. Monolayer–bilayer junctions at a double-height step provide the highest resistance seen here, 88 Ω μm.

We find that the upper graphene layer is continuous over the monolayer–bilayer junction (Supplementary Fig. S1b), consistent with other reports[14]. Given the continuous nature of the graphene sheet, the substantial resistance of the junction is perhaps counter-intuitive, and might suggest the presence of defects or scatterers at the graphene edge. To understand this, we calculated the resistance

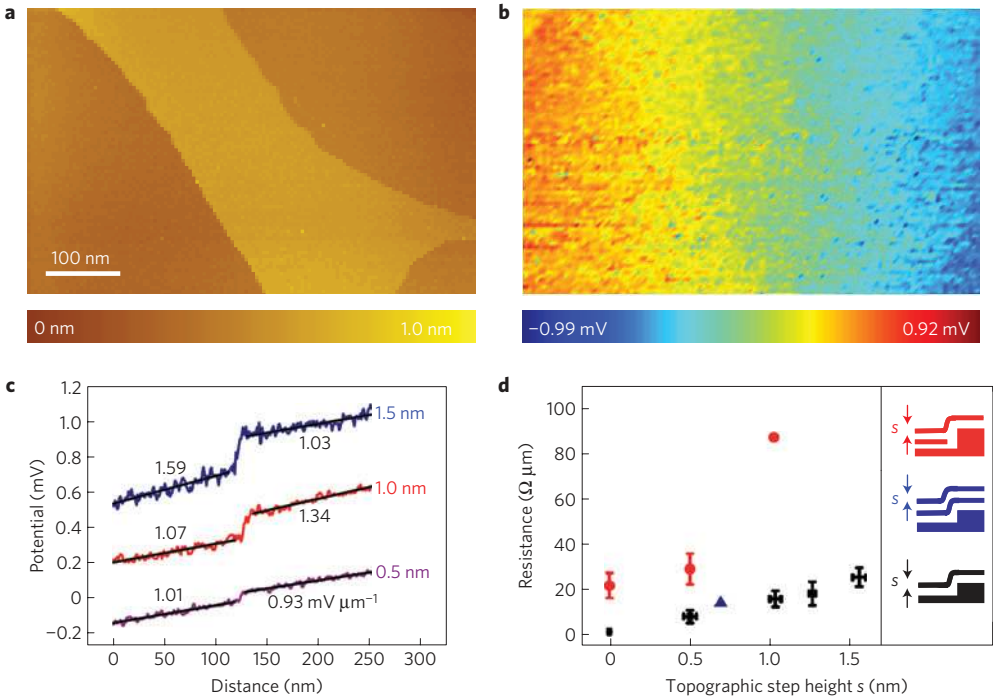

Figure 3 | Single-layer graphene overlaying substrate steps. a,**b**, STM topography (**a**) and scanning tunnelling potentiometry (**b**) recorded simultaneously at $V_{13} = -1.53$ V; data measured at low temperature (~72 K) to reduce scan noise. The local current density is 6.4×10^{-6} A μm^{-1}. **c**, Potential profiles of monolayer graphene over single-, double- and triple-height substrate steps. The values of the terrace gradients are indicated to give an idea of variability in the data and enable us to calculate that 0.5, 1.0 and 1.5 nm steps contribute resistance equivalent to ~40, 80 and 120 nm of monolayer terrace width respectively. **d**, The resistance of configurations with different numbers of layers and topographic step heights *s*. Inset diagrams show the configuration, with the buffer layer omitted for clarity. The bilayer is typically at the lower terrace. All data were obtained at low temperature except for the bilayer (triangular) data point, and all data are from the low-miscut sample except for the 88 Ω μm data point, which is from a different but nominally identical sample, and the bilayer data point, which is from the high-miscut sample. For monolayer graphene over 0.5, 1.0, 1.25 and 1.5 nm steps, seven, five, two and three steps respectively were measured. For monolayer–bilayer junctions with 0 and 0.5 nm topographic height changes, two and five steps respectively were measured. Vertical and horizontal error bars are root mean squared values calculated from variations in resistance and in measured step height respectively. For the 88 Ω μm data point only one step was measured and no error bar is shown.

using a standard tight-binding model of the monolayer and bilayer wavefunctions[21]. For energies near the Dirac point, a continuum approximation is generally considered adequate[22,23]. However, in view of the considerable doping here, we use a full atomistic approach with exact boundary conditions (effectively equivalent to the non-equilibrium Green function approach used for overlapping nanoribbons[24]; see Supplementary Information for details). The model has five parameters: in-plane and interlayer matrix elements t, bilayer bandgap Δ and the respective doping levels E_F, all of which are known for epitaxial graphene on SiC (refs 19,21). With these values ($t_{in-plane} = 3.1$ eV, $t_{interlayer} = 0.4$ eV, $E_F = 0.45$ eV in monolayer, 0.3 eV in bilayer, $\Delta = 0.15$ eV), we calculate resistances ~25 Ω μm and ~14 Ω μm for junctions with armchair and zigzag orientation, respectively. The junction measured has predominantly armchair orientation. The agreement between calculated and measured values is striking, although this could be partly fortuitous given the uncertainties in doping level and bandgap. These results clearly show that a high resistance is an intrinsic property of an ideal monolayer–bilayer junction.

The 25 Ω μm resistance corresponds to an average transmission factor of $T \approx \frac{1}{2}$, consistent with that found at low doping[22,23]. We find that the poor transmission is largely a result of the wavefunction mismatch between monolayer and bilayer, unavoidable because the bilayer wavefunctions have large amplitude on both layers: wavefunction matching requires intermixing with an evanescent state from a higher-energy band of the bilayer. Thus, wavefunction mismatch is an inherent characteristic of this interface, and calculations using standard methods confirm that this inherent mismatch is sufficient to account for the magnitude of resistance observed experimentally. We also find considerable interband (K–K′) scattering for the armchair orientation, so chirality is not conserved[13]. Even for the zigzag orientation, where by symmetry there is no K–K′ scattering, there is still a strong wavefunction mismatch; and the calculations suggest a large resistance, although the conservation of chirality for the zigzag orientation contributes to the lower resistance when compared with the armchair orientation.

For a continuous graphene layer going over a substrate step, we suggest that the origin of the step-induced resistance may be intrinsic, induced for example by σ–π hybridization arising from the curvature of the graphene sheet near the top and bottom of the step.

The combination of potential mapping and modelling has thus shown that substrate steps, terraces and thickness changes all contribute to the resistance. Each element can be treated as following Ohm's law at the nanoscale. Steps and junctions strongly affect transport. A 0.5 nm substrate step contributes extra resistance equivalent to a ~40-nm-wide terrace. 1.0- and 1.5-nm-high substrate steps contribute resistance equivalent to ~80 and ~120 nm of terrace respectively, and monolayer–bilayer junctions contribute ~100 nm or more. We can verify this understanding of current flow by simulating the potential distribution across the sample. In Fig. 2g,h, we show a simulation with fixed boundary potentials taken from the experimental data in Fig. 2a–f. The results are in close agreement with the data, enabling resistances to be estimated that are consistent with the values obtained above from analysis of line profiles.

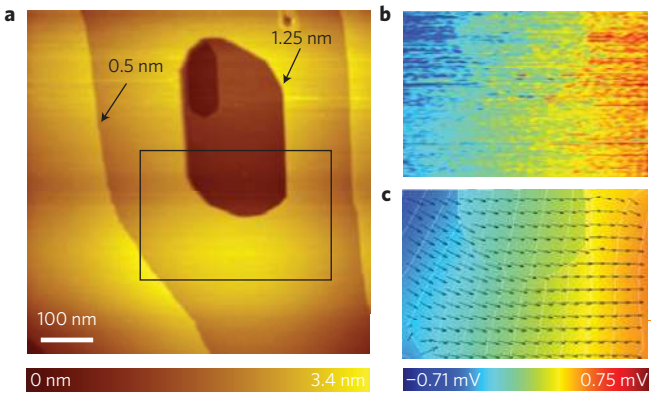

Figure 4 | Details of current flow around steps. a, Topography of monolayer graphene across substrate steps and a 1.25-nm-deep vacancy island ($V = 0.2$ V, $I = 0.1$ nA). **b**, Potential map (385 nm × 264 nm, $V_{13} = 1.53$ V, $V_{a.c.} = 2$ mV, $I = 50$ pA). **c**, Simulation of the same region showing equipotential contours and electron flow (arrows). The local current density is 6.9×10^{-6} A μm^{-1}.

Macroscopic conductivity measurements thus provide only a small part of the full picture required to understand transport through graphene on SiC. Miscut steps, islands formed during the growth process and thickness variations will all reduce the macroscopic conductivity. For example, the two samples in Table 1 show similar (within 11%) local conductivities measured on single terraces. Yet in the high-miscut sample the macroscopic conductivity was ∼3× lower than the local value, whereas the low-miscut sample showed a difference of only ×1.2. Steps from even a 0.7° miscut should double the resistance in the miscut direction and lead to anisotropy in transport, as already seen by four-probe measurements[25]. We believe that these results are also relevant to graphene on other substrates. Local variations in conductivity have already been seen within and between graphene flakes on SiO_2 (ref. 26). But even for a structurally perfect graphene layer, substrate-induced steps may reduce mobility on substrates such as mica[27] and boron nitride[28]. As the properties and processing of dielectrics such as SiO_2 are improved, the effects of thickness changes and distortions to the graphene sheet will become more important in determining device properties.

We finally consider the possibilities suggested by local control of current flow. The steps and boundaries analysed so far were generally perpendicular to the current. In Fig. 4a we show how current flows in two dimensions when the resistive features have a more complex geometry, here a closed loop. Such features distort the flow of current (Fig. 4b), as seen in the simulated equipotential contours and the small reduction in current density inside the island (Fig. 4c). It is interesting to speculate whether spatial control of step configurations could be used to concentrate current into specific regions of a graphene sheet for new device designs.

Methods

Graphene growth and imaging. Growth of graphene layers took place in an ultrahigh-vacuum low-energy electron microscope, electron-beam heating the sample to 1,300 °C while exposing undoped Si-terminated SiC(0001) wafers to 5×10^{-6} torr disilane[29,30]. The instrument used was the IBM LEEM-II (refs 29,30). Growth *in situ* enabled the step density and configuration of the sample to be determined and the graphene thickness monitored during and after growth. Growth was terminated when samples showed large area fractions of monolayer graphene as well as smaller fractions of bilayer graphene. Some samples also contained lithographically defined patterns so that the same areas could be imaged in LEEM and STM. After graphene growth, samples were transferred through air to an ultrahigh-vacuum system containing a four-probe, low-temperature scanning tunnelling microscope and a scanning electron microscope. The scanning tunnelling microscope is a Unisoku UHV-LT four-probe, low-temperature scanning tunnelling microscope operated with an RHK SPM-1000 controller. Scanning electron microscopy images were acquired using an FEI 2LE Schottky column. Brief heating to 600 °C in a preparation chamber was used to desorb species such as water before loading into the STM stage. Scanning tunnelling microscopy and spectroscopy as well as scanning tunnelling potentiometry[15,16] were then carried out, either at room temperature or at 72 K. In scanning tunnelling potentiometry, two probes set up a potential difference between two points on the sample, while a third probe measures the local potential between the two probes. The local potential is determined in a tunnelling experiment, by measuring the condition in which no tunnelling current flows (that is zero potential difference between the tip and the location on the sample at which the tip is positioned). Contact potential thus does not play a role. Furthermore, the contact resistance at the fixed probes only determines the potential drop at the contact regions and has no effect on results from local potential measurement. The data were acquired with a PtIr tip, cleaned *in situ* by approaching a metallic target while applying a high electric field, and using home-built electronics based on the circuit described in ref. 15.

Macroscale conductivity measurement. We assume that the graphene sheet has a uniform conductivity on the macroscale. In this two-dimensional system, the voltage on the surface should satisfy $\nabla^2 V = 0$. Assuming point contacts for the fixed probes, and taking the probe positions as $(d/2, 0)$ and $(-d/2, 0)$ and $V = 0$ at the origin, the distribution of the potential is

$$V(x,y) = A \ln\left(\frac{\sqrt{(x+(d/2))^2+y^2}}{\sqrt{(x-(d/2))^2+y^2}}\right) \quad (1)$$

Integrating the current density along the y axis, we obtain the total current

$$I = \int_{-\infty}^{+\infty} \frac{\partial}{\partial x} V(0,y)\sigma_{avg}\,dy = \int_{-\infty}^{+\infty} A\frac{d}{(d/2)^2+y^2}\sigma_{avg}\,dy = 2\pi A\sigma_{avg}$$

where σ_{avg} is the 'macroscopic' conductivity and A is a fitting constant with units of voltage.

Finally, the 'macroscopic' current density at the origin is given by

$$j = \frac{4A\sigma_{avg}}{d} = \frac{2I}{\pi d}$$

We measure V in several places by stepping probe 2 along the line between probes 1 and 3. Fitting the V values to equation (1) yields a value for A. We also measure d and I directly. From A, d and I, we obtain the values for σ_{avg} and j used in the analysis. In reality, the contact tips have finite size and irregular shape, within which the potential is constant. The voltage difference between the two contacts is V_{13}. To fit equation (1) we assume circular contacts of diameter ∼60 μm estimated from scanning electron microscopy.

Received 11 July 2011; accepted 13 October 2011; published online 20 November 2011

References

1. Novoselov, K. S. *et al.* Two-dimensional gas of massless Dirac fermions in graphene. *Nature* **438,** 197–200 (2005).
2. Zhang, Y. B., Tan, Y-W., Stormer, H. L. & Kim, P. Experimental observation of the quantum Hall effect and Berry's phase in graphene. *Nature* **438,** 201–204 (2005).
3. Berger, C. *et al.* Electronic confinement and coherence in patterned epitaxial graphene. *Science* **312,** 1191–1196 (2006).
4. Avouris, P. Graphene: Electronic and photonic properties and devices. *Nano Lett.* **10,** 4285–4294 (2010).
5. Du, X., Skachko, I., Barker, A. & Andrei, E. Y. Approaching ballistic transport in suspended graphene. *Nature Nanotech.* **3,** 491–495 (2008).
6. Bolotin, K. I., Sikes, K. J., Hone, J., Stormer, H. L. & Kim, P. Temperature-dependent transport in suspended graphene. *Phys. Rev. Lett.* **101,** 096802 (2008).
7. Chen, J-H. *et al.* Intrinsic and extrinsic performance limits of graphene devices on SiO_2. *Nature Nanotech.* **3,** 206–209 (2008).
8. Ando, T. Screening effect and impurity scattering in monolayer graphene. *J. Phys. Soc. Jpn* **75,** 074716 (2006).
9. Hwang, E. H., Adam, S. & Das Sarma, S. Carrier transport in two-dimensional graphene layers. *Phys. Rev. Lett.* **98,** 186806 (2007).
10. Cheianov, V. & Fal'ko, V. I. Friedel oscillations, impurity scattering, and temperature dependence of resistivity in graphene. *Phys. Rev. Lett.* **97,** 226801 (2006).
11. Hibino, H. *et al.* Microscopic thickness determination of thin graphite films formed on SiC from quantized oscillation in reflectivity of low-energy electrons. *Phys. Rev. B* **77,** 075413 (2008).
12. Mallet, P. *et al.* Electron states of mono- and bilayer graphene on SiC probed by scanning-tunnelling microscopy. *Phys. Rev. B* **76,** 041403(R) (2007).
13. Rutter, G. M. *et al.* Scattering and interference in epitaxial graphene. *Science* **317,** 219–222 (2007).

14. Lauffer, P. *et al.* Atomic and electronic structure of few-layer graphene on SiC(0001) studied with scanning tunnelling microscopy and spectroscopy. *Phys. Rev. B* **77,** 155426 (2008).
15. Bannani, A., Bobisch, C. A. & Möller, R. Local potentiometry using a multiprobe scanning tunnelling microscope. *Rev. Sci. Intrum.* **79,** 083704 (2008).
16. Homoth, J. *et al.* Electronic transport on the nanoscale: Ballistic transmission and Ohm's law. *Nano Lett.* **9,** 1588–1592 (2009).
17. Rutter, G. M. *et al.* Imaging the interface of epitaxial graphene with silicon carbide via scanning tunnelling microscopy. *Phys. Rev. B* **76,** 235416 (2007).
18. Ohta, T. *et al.* Interlayer interaction and electronic screening in multilayer graphene investigated with angle-resolved photoemission spectroscopy. *Phys. Rev. Lett.* **98,** 206802 (2007).
19. Zhou, S. Y. *et al.* Substrate-induced bandgap opening in epitaxial graphene. *Nature Mater.* **6,** 770–775 (2007).
20. Nagase, M., Hibino, H., Kageshima, H. & Yamaguchi, H. Local conductance measurements of double-layer graphene on SiC substrate. *Nanotechnology* **20,** 445704 (2009).
21. Castro Neto, A. H., Guinea, F., Peres, N. M. R., Novoselov, K. S. & Geim, A. K. The electronic properties of graphene. *Rev. Mod. Phys.* **81,** 109–162 (2009).
22. Nilsson, J., Castro Neto, A. H., Guinea, F. & Peres, N. M. R. Transmission through a biased graphene bilayer barrier. *Phys. Rev. B* **76,** 165416 (2007).
23. Nakanishi, T., Koshino, M. & Ando, T. Transmission through a boundary between monolayer and bilayer graphene. *Phys. Rev. B* **82,** 125428 (2010).
24. González, J. W., Santos, H., Pacheco, M., Chico, L. & Brey, L. Electronic transport through bilayer graphene flakes. *Phys. Rev. B* **81,** 195406 (2010).
25. Yakes, M. K. *et al.* Conductance anisotropy in epitaxial graphene sheets generated by substrate interactions. *Nano Lett.* **10,** 1559–1562 (2010).
26. Nirmalraj, P. N. *et al.* Nanoscale mapping of electrical resistivity and connectivity in graphene strips and networks. *Nano Lett.* **11,** 16–22 (2011).
27. Lui, C. H., Liu, L., Mak, K. F., Flynn, G. W. & Heinz, T. F. Ultraflat graphene. *Nature* **462,** 339–341 (2009).
28. Dean, C. R. *et al.* Boron nitride substrates for high-quality graphene electronics. *Nature Nanotech.* **5,** 722–726 (2010).
29. Tromp, R. M. & Hannon, J. B. Thermodynamics and kinetics of graphene growth on SiC(0001). *Phys. Rev. Lett.* **102,** 106104 (2009).
30. Hannon, J. B. & Tromp, R. M. Pit formation during graphene synthesis on SiC(0001): *In situ* electron microscopy. *Phys. Rev. B* **77,** 241404(R) (2008).

Acknowledgements

We thank A. Ellis and M. C. Reuter of IBM for their assistance with experimental aspects of this work, and R. Möller and X. Chen for discussions.

Author contributions

S-H.J. carried out scanning tunnelling potentiometry experiments, J.B.H. and R.M.T. grew the graphene and carried out LEEM; J.T. and V.P. carried out the calculations; S-H.J., F.M.R., J.B.H. and R.M.T. collaborated on equipment and experimental design; all authors wrote the paper.

Additional information

The authors declare no competing financial interests. Supplementary information accompanies this paper on www.nature.com/naturematerials. Reprints and permissions information is available online at http://www.nature.com/reprints. Correspondence and requests for materials should be addressed to S-H.J. or F.M.R.